RESEARCH ARTICLE

Effect of low voltage limit on degradation mechanism during high-frequency dynamic load in proton exchange membrane water electrolysis

Anastasiia Voronova[1,2] | Hyoung-Juhn Kim[1] | Jong Hyun Jang[1,2] |
Hee-Young Park[1] | Bora Seo[1,2] (iD)

[1]Hydrogen and Fuel Cell Research Center, Korea Institute of Science and Technology (KIST), Seoul, Republic of Korea

[2]Division of Energy & Environment Technology, KIST School, University of Science and Technology (UST), Seoul, Republic of Korea

Correspondence
Hee-Young Park and Bora Seo, Hydrogen and Fuel Cell Research Center, Korea Institute of Science and Technology (KIST), Seongbuk-gu, Seoul 02792, Republic of Korea.
Email: parkhy@kist.re.kr (H.-Y. P.) and brseo@kist.re.kr (B. S.).

Summary

With regard to the hydrogen economy, setting the criteria for the durability evaluation of renewable energy-powered proton exchange membrane water electrolysis (PEMWE) systems is an important milestone. In this study, accelerated stress test (AST) protocols that simulate the fluctuating power supply of renewable energy were explored. The average load was varied by changing the low voltage limit (LVL = 1.4, 1.5, 1.7, and 1.9 V) with fixation of a high voltage limit of 2.2 V. AST protocols can accurately reflect the real solar profile with various loads and high ramp rates. Protocols with the LVL = 1.4 V and LVL = 1.5 V demonstrated opposite trends even with minimal difference in LVL, resulting in positive and negative degradation slopes, respectively. The positive degradation slope (meaning performance decrease) for LVL 1.4 V is attributed to the reversal current, resulting in degradation of the cathode catalyst, which is characteristic of the fuel cell operating mode. On the contrary, a slight performance increase was observed for LVL 1.5 V, presumably caused by the thinning of the membrane and the creation of a rougher surface in the anode/membrane interface. Meanwhile, protocols with higher LVL (LVL 1.7 V and LVL 1.9 V) showed significant mass transport loss observed at voltages larger than 1.8 V. This may be attributed to severe delamination of the catalyst/membrane and/or diffuse layer/catalyst interface, presumably due to the changes in bubble nucleation and the resulting stress. The findings suggest a rational guideline for establishing a unified AST protocol applicable to renewable energy-powered PEMWE systems, and subsequent material development strategies to minimize degradation processes.

KEYWORDS
accelerated stress test, degradation mechanism, high frequency cycling, low voltage limit, membrane electrode assembly, proton exchange membrane water electrolysis, renewable energy

1 | INTRODUCTION

With the advantages of load flexibility, high efficiency, and low environmental impact, proton exchange membrane water electrolysis (PEMWE) powered by renewable energy sources has attracted considerable research attention as a key component for a future hydrogen energy society.[1,2] The practical implementation of the system necessitates a comprehensive understanding of the degradation mechanisms that occur in the membrane electrode assembly (MEA) under fluctuating power supply because of the intermittent nature of renewable sources.[3] In the case of coupling with the wind energy supply, the frequency of the wind energy spikes occurring is 1 to 2 Hz and photovoltaic power fluctuation is even higher, typically in the range of 0.5 to 0.1 Hz.[4] Solar irradiance profiles obtained during PEM water electrolysis coupled with a photovoltaic panel demonstrate the frequent variation of solar irradiance and, subsequently, stack current.[5,6]

Various accelerated stress test (AST) protocols have been proposed and investigated to evaluate the durability and corresponding degradation mechanism of the renewable energy-powered PEMWE system in a relatively short period (Table S1). In this regard, in the NEXPEL project (Next-Generation PEM Electrolyzer for Sustainable Hydrogen Production), single cells and stacks were optimized and used to investigate degradation processes in a subsequent NOVEL project,[7,8] where three types of AST protocols with square-wave profiles were suggested to accelerate membrane thinning and Ti passivation at a given time. Among them, the AST profile that stresses target components to the greatest extent and, accordingly, resulted in the highest degradation slope has been proposed as the best aging protocol.[8] Another completed project, named ELECTROHYPEM, focused primarily on investigating the aging process under a protocol simulating wind profile, which showed fairly low degradation slopes, probably because of the use of stable materials and low operating current densities.[9] Unfortunately, the major degradation processes were not identified in this study.

In addition, various stress test protocols have been provided by ongoing projects. H2future project developed an AST protocol that investigates the system behavior under start/stop sequences and partial/full load operating conditions to implement a PEM water electrolyzer into grid services.[10] The HPEM2GAS project, implementing results from previous projects, deals with the AST protocols for evaluating the performance, durability, efficiency, and dynamic behavior of electrolyzer systems. In particular, an AST protocol aimed at anode catalyst degradation was developed with specific regard to assessing its operation in a grid-balancing service.[4] However, it is difficult to derive consistent conclusions for the degradation processes given the high variability in the protocol conditions and sample compositions. Therefore, a detailed exploration of the prevailing degradation mechanisms under certain AST conditions is important.

In this regard, recent academic reports aim to investigate durability and stability measurements (Table S2) based on dynamic cycling protocols with a step duration ranging from several minutes to tens of hours. Shorter step durations are less studied and are a necessary research topic, considering the high ramp rate events that occurred during the operation of renewable sources.[11-14] In addition, there is considerable attention toward the influence of high current density operation, which reduces the system cost. However, it remains unknown how this affects long-term stability.[15-17] Fouda-Onana et al[18] suggested dynamic voltage cycling that does not exceed a nominal load of 1 A cm^{-2}, assuming membrane thinning by a radical attack and Ti passivation as major degradation processes at 60°C and 80°C, respectively. In the research conducted by Rozain et al,[19] an AST protocol based on the square-wave profile with a current step from 0 to 2 A cm^{-2} was applied to mimic a real solar-type profile. In addition to the aforementioned membrane thinning and Ti passivation, the authors point out that catalyst layer degradation can be induced by rapid oxygen nucleation at higher current densities as the most influential degradation process.

In dynamic operation, the open-circuit voltage (OCV) period has a significant influence on the degradation process. Weiss et al[20] proposed that repetitive switching between oxidation and reduction during dynamic cycling passing through OCV multiple times increases the Ir dissolution, thereby increasing the degradation slope. No degradation was observed for dynamic cycling without OCV periods. These results contradict the findings of Rakousky et al,[21] who observed a higher degradation slope with dynamic operation from 1 to 2 A cm^{-2} compared to the operation from 0 to 2 A cm^{-2}, including the OCV period. The discrepancies possibly originated from the differences in the materials used (electrode, membranes, and porous transport layers), operating conditions (temperature and operation time), and dynamic profiles used (step duration and number of cycles). Li et al[22] emphasized the cathode degradation as the main degradation process during 0 A cm^{-2} (OCV) to 0.5 A cm^{-2} cycling, assuming carbon cloth corrosion and Pt dissolution occurred in case of low loads operation, which includes the OCV period.

The dynamic load frequency and applied load limits also contributed to the degradation rate. Rakousky et al demonstrated that dynamic loads with step durations of

6 hours and 10 minutes slightly reduced the degradation by reducing reversible* losses compared to the steady-state test.[21] Indeed, the steady-state test at 2 A cm^{-2} showed the highest degradation value among the investigated protocols, and the same trend was observed by Hegge et al[11] and Frensch et al[23] Siracusano et al[12] reached a similar conclusion, highlighting performance decay mitigation due to reversible losses. This study also suggested that the dynamic protocol could restore the catalytic properties by changing the oxidation states on the catalyst surface. Frensch et al,[23] investigating the influence of dynamic operation modes with step durations of 20, 120, and 200 seconds in comparison with the steady-state operation mode, found a slight performance increase for fast cycling dynamic mode (20 and 120 seconds), mainly due to a decrease in high-frequency resistance (HFR). According to their findings, increased fluoride emission was observed for fast cycling modes, along with the catalyst structure adjustment accompanied by an increase in anodic charge.

Considering the applied load limits, Babic et al[13] investigated the influence of upper voltage load in a dynamic mode with a step duration of 60 seconds. The on-state cell voltage varied between 1.8 and 2.2 V during cycling. This work revealed that a higher degree of iridium oxide dissolution was present at higher applied voltages (more pronounced for OCV −2.2 V cycling in comparison with OCV −1.8 V cycling), which was observed in previous rotating disk electrolysis experiments,[14,24] but the iridium loss did not cause any significant increase in the kinetic losses due to initially high catalyst loading.

Figure 1 shows the summarized degradation rates (mV h^{-1}) measured using dynamic AST protocols. Considering that membrane thinning[12,18,22,24,25] and Ti passivation[18,20-22] are frequently specified as the main degradation mechanisms, the type of membrane used and the presence of Pt coating on Ti porous transport layer (PTL) are indicated in the inset box. In addition, considering the significant impact of Ir dissolution on the degradation in the case of low catalyst loading under high load dynamic operation,[13,14,21,22] the anode catalyst loading was also indicated. All other details of the tests are described in Data S1 (Tables S1 and S2). This demonstrates that among dynamic load studies, negative degradation slopes were observed for protocols with short step duration cycling, thereby demonstrating a temporary performance increase due to membrane thinning and the evolution of rougher surfaces by catalyst dissolution.[13,23] However, structural changes in MEA and membrane thinning, which have a positive effect at the outset, can lead to rapid cell failure during prolonged operation. It is worth mentioning that dynamic protocols tend to show a decreased degradation rate compared to steady-state
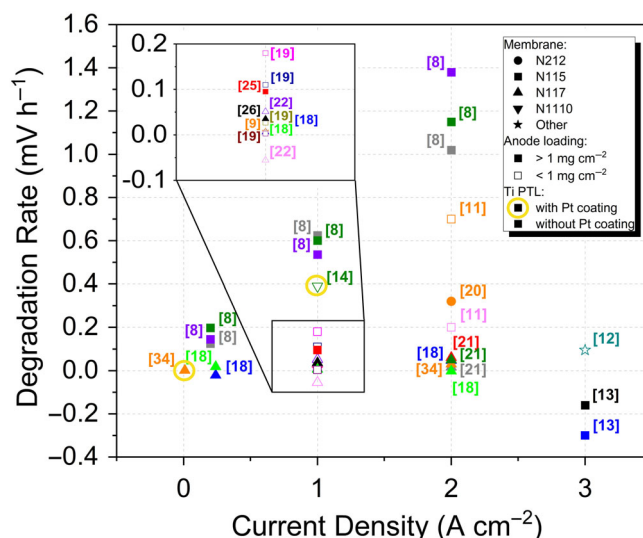

FIGURE 1 Reported degradation rates under dynamic AST protocols

protocols.[13,21,23] Positive degradation slopes have mostly been explained by Ti PTL passivation,[18,19,21,22] cathode degradation during cycling to the OCV,[21,22] and agglomeration and migration of Ir catalysts.[14,26] Thus, the data on degradation processes triggered by dynamic loads are scattered and material-dependent. This implies that a certain dynamic protocol to evaluate system stability and durability has not yet been established.

In this study, a dynamic AST protocol adapted from the HPEM2Gas project, with cycling limits from 1.4 to 2.2 V, a sweep rate of 150 mV s^{-1}, and a short step duration of 10 seconds was used. As the real solar irradiance profiles feature highly fluctuating and various loads, which rely on the weather (Figure S1,[27]), we investigated the influence of applied loads by changing the lower voltage limit (LVL) to 1.5, 1.7, and 1.9 V, while maintaining the upper voltage limit (UVL, 2.2 V) and sweep rate. The conditions reflect fluctuating and high loads, which are typical for highly variable irradiance profiles. Protocols with LVL = 1.4 V and LVL = 1.5 V showed opposite results, demonstrating positive, and negative degradation slopes, respectively. The positive degradation slope (meaning performance decrease) for LVL 1.4 V is attributed to the reversal current, causing degradation of Pt/C catalyst in the cathode, characteristic of the fuel cell operating mode. On the contrary, a marginal performance increase was observed for LVL 1.5 V, which was most likely caused by the membrane thinning and the generation of a rough surface by catalyst dissolution in the anode. Meanwhile, protocols with higher LVL (LVL 1.7 V and LVL 1.9 V) showed significant mass transport losses observed at voltages larger than 1.8 V, which may be attributed to severe delamination of the catalyst/membrane and/or diffuse layer/catalyst interface,

probably due to bubble growth and the resulting stress. These results offer a way to establish a unified AST protocol applicable to renewable energy-powered PEMWE and material development strategies to minimize degradation processes.

2 | EXPERIMENTAL

2.1 | MEA preparation and test bench setup

Used as a solid electrolyte, Nafion N115 membrane, with a typical thickness of 127 μm and a conductivity of 0.1 S cm^{-1} was preliminarily protonated in 0.5 M H$_2$SO$_4$ at 80°C for 1 hour. To remove excess acid, the membrane was immersed in distilled water (1 hour, 80°C), then repeatedly rinsed until neutral pH and dried at 60°C for 12 hours. Catalyst inks were ultrasonically sprayed onto the membrane (NanoNC Electrospray Machine, Sono Tek Ultrasonic Spray Platform). IrO$_2$ (Alfa Aesar, 99.99% metal basis) and Pt/C (Tanaka Kikinzoku Int., 46.6% Pt) were used as the anode and cathode catalysts, respectively. Spraying inks were prepared as follows: catalyst powder and Nafion ionomer (Sigma Aldrich, 5 wt% solution) were ultrasonically dispersed for 30 minutes in a deionized water/isopropanol solution and the obtained suspension was subsequently mixed for 1 hour. The obtained catalyst inks were then ultrasonically sprayed directly onto the membrane, resulting in catalyst loadings of 1 mg cm^{-2} on both the cathode and anode. The catalyst coated membrane (CCM) was then hot-pressed (80°C, 2 minutes, 1 m.t.) with a Ti felt (Bekaert/2GDL8N-025N, 250 μm thickness, 65% porosity[28]) as the anode diffuse layer and carbon paper (SGL carbon/39BC, 325 ± 25 μm thickness, 80% porosity[29]) as the cathode diffuse layer. The anode diffuse layer was preliminarily etched in oxalic acid (65°C, 0.5 hour) to remove the oxide film. The obtained MEA was assembled in a 4 cm^2 cell with a Pt-coated Ti anode flow field and graphite cathode flow field, and the clamping force was set to 70 Lb. A schematic of the cell components is shown in Figure 2. A total of 12 samples were tested, with three samples per AST protocol, to ensure reproducible data.

2.2 | AST protocol and electrochemical characterization

The assembled cell was subjected to the AST protocol, consisting of the beginning of the test (BoT) experiment sequence, potentiodynamic cycling as an AST, and end of the test (EoT) experiment sequence, as depicted in
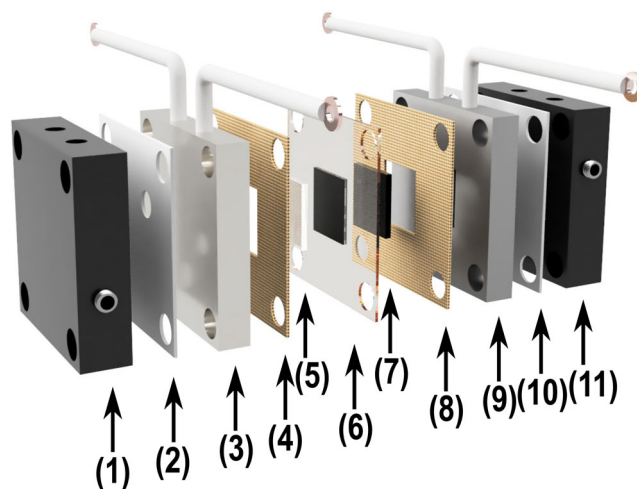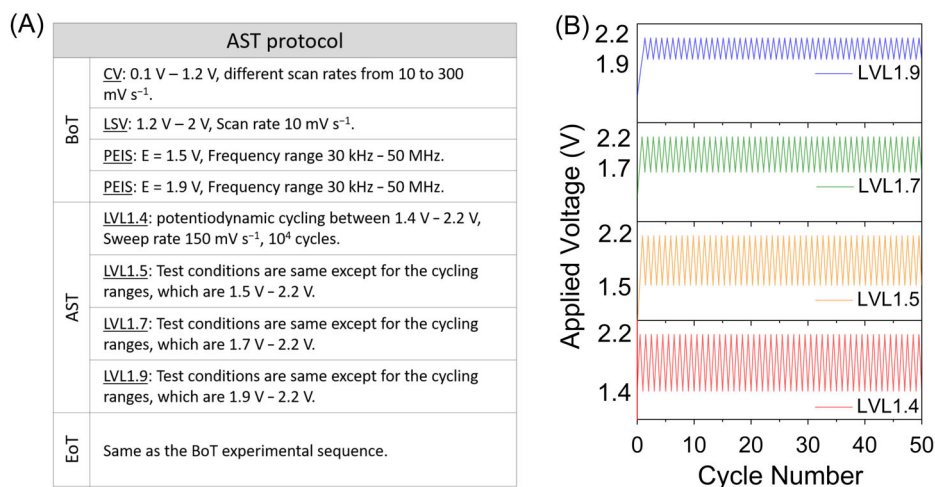

FIGURE 2 Schematic description of electrolysis cell: (1) anode endplate, (2) anode isolation layer, (3) anode Ti/Pt flow field, (4) anode gasket, (5) anode PTL Ti felt, (6) CCM with the IrO$_2$ catalyst layer at the anode and Pt/C catalyst layer at the cathode, (7) cathode PTL carbon paper, (8) cathode gasket, (9) cathode flow field, (10) cathode isolation layer, and (11) cathode endplate

Figure 3A. Single-cell experiments were performed using a commercial test station (water electrolysis system, CNL Energy, Korea) and a high-current potentiostat/galvanostat with electrochemical impedance spectroscopy (EIS) (Bio-Logic, HCP-803). Nitrogen-saturated deionized water (18.2 MΩ), as a reactant and temperature control medium, was circulated through the anode compartment with a flow rate of 15 mL min^{-1}. The cell temperature was maintained at 80°C by preheating the inlet water media and in-cell cartridge heaters. As the BoT and EoT experiments sequence, cyclic voltammetry, linear sweep voltammetry (LSV), and EIS were performed. Cyclic voltammograms (CVs) were recorded in a voltage range from 0.1 to 1.2 V at different scan rates (from 10 to 300 mV s^{-1}). During cyclic voltammetry, a nitrogen-saturated water flow was pumped through the anode compartment, and the H$_2$ atmosphere was set at the cathode, which was used as both the counter and reference electrode. Polarization curves were recorded from 1.2 to 2.2 V after an activation time of 30 minutes at 1.55 V. EIS measurements were carried out at the frequency ranges from 30 kHz to 50 MHz and at two voltages of 1.5 V (mainly affected by catalytic activity) and 1.9 V (including the effect of mass transport).

To investigate the influence of the LVL, the samples were tested under four different AST protocols (Figure 3B). As the reference used specifically aimed at the anode degradation protocol, proposed by HPEM2Gas[4] (potentiodynamic cycling between 1.4 and 2.2 V with a sweep rate of 150 mV s^{-1} for 10^4 cycles, which results in a cycle duration of 10 seconds). The LVL was changed to 1.5, 1.7, and 1.9 V for other protocols.

FIGURE 3 AST protocol. (A) Experimental sequence with test conditions. (B) Applied voltage profiles (profiles only for 50 cycles are presented in the figure; the total cycle number was 10 000)

(A)

AST protocol	
BoT	<u>CV</u>: 0.1 V – 1.2 V, different scan rates from 10 to 300 mV s⁻¹.
	<u>LSV</u>: 1.2 V – 2 V, Scan rate 10 mV s⁻¹.
	<u>PEIS</u>: E = 1.5 V, Frequency range 30 kHz – 50 MHz.
	<u>PEIS</u>: E = 1.9 V, Frequency range 30 kHz – 50 MHz.
AST	<u>LVL1.4</u>: potentiodynamic cycling between 1.4 V – 2.2 V, Sweep rate 150 mV s⁻¹, 10⁴ cycles.
	<u>LVL1.5</u>: Test conditions are same except for the cycling ranges, which are 1.5 V – 2.2 V.
	<u>LVL1.7</u>: Test conditions are same except for the cycling ranges, which are 1.7 V – 2.2 V.
	<u>LVL1.9</u>: Test conditions are same except for the cycling ranges, which are 1.9 V – 2.2 V.
EoT	Same as the BoT experimental sequence.

2.3 | Physicochemical characterization

To provide additional insight into the degradation processes that occurred, field-emission scanning electron microscopy (FEI Inspect F, accelerating voltage of 20 kV) images of the MEA cross-section were taken before (individual sample was disassembled from the cell after the conditioning procedure and cut, giving the BoT cross-sectional image. Preliminary conditioning was performed to consider the influence of clamping and swelling on the membrane thickness) and after the AST. Cross-sections of the MEA samples were obtained using a cryo-ion-milling system (ArBlade 5000, Hitachi High-Tech). In addition, X-ray photoelectron spectroscopy (XPS, PHI 5000, VersaProbe, equipped with a monochromatic Al K$_\alpha$ X-ray source [1486.6 eV]) was performed to provide a comparative assessment of the Ti PTL passivation degree. For the analysis, a square-shaped piece of Ti PTL (0.5 by 0.5 cm) was taken from the middle of the sample of each series and the side adjacent to the catalytic layer was analyzed. The curve fitting of the XPS spectra was performed using XPSpeak41 software. The baseline of the XPS spectra was corrected using the Shirley-type background with a zero slope, and the full-width-at-half-maximum values were constrained to 2.5 eV for the main peaks.

3 | RESULTS AND DISCUSSION

3.1 | Cell performance changes

The degradation processes were assessed by reflecting the overpotential contributions from different regions of the polarization curves. The overall cell voltage can be described as the sum of the equilibrium potential and overpotentials associated with irreversible losses[30]:

$$V_{cell} = E_{rev} + \eta_{act,an} + \eta_{act,cat} + \eta_{ohm} + \eta_{diff,an} + \eta_{diff,cat} + \eta_{bubble,an} \quad (1)$$

where E_{rev} is the reversible potential; $\eta_{act,an}$ and $\eta_{act,cat}$ are the anode and cathode activation overpotentials, respectively; $\eta_{diff,an}$ and $\eta_{diff,cat}$ are the anode and cathode diffusion overpotentials, respectively, and $\eta_{bubble,an}$ is the anode bubble overpotential. Taking into account fast cathode kinetics and correspondingly low $\eta_{act,cat}$[31] and also combining $\eta_{diff,an}$, $\eta_{diff,cat}$, and $\eta_{bubble,an}$ as mass transport overpotential η_{mt},[30] Equation (1) can be simplified to:

$$V_{cell} = E_{rev} + \eta_{kin} + \eta_{ohm} + \eta_{mt} \quad (2)$$

where cell overpotentials are described as kinetic overpotential η_{kin}, ohmic overpotential η_{ohm}, and mass transport overpotential η_{mt}. Kinetic overpotential can be defined from the low current densities region (10-100 mA cm⁻², no mass transport overpotential is expected) by the Tafel fitting in the linear region:

$$\eta_{kin} = b \cdot \log\left(\frac{j}{j_0}\right) \quad (3)$$

where b is the Tafel slope and j_0 is the apparent current density. In turn, ohmic overpotential η_{ohm} can be calculated using the HFR value, and mass transport overpotential η_{mt} can be defined as the difference between the Tafel line and the iR-free cell voltage[32]:

$$\eta_{mt} = E_{rev} - \eta_{kin} - \eta_{ohm} \quad (4)$$

Thus, the constituents of the cell voltage were calculated and the corresponding polarization curves breakdown

can be seen in Figure S2-S5. Averaged polarization curves for each set of samples can be seen in Figure S6.

To investigate the peculiarities of the current density profile during the stress test, the current densities at the UVL (2.2 V) were plotted against the AST cycle number (Figure 4A) to reflect the performance decay dynamic during the AST. As can be seen, for the LVL 1.9 and LVL 1.7 samples, the current density profile can be conditionally divided into two regions: the initial region with a high degradation slope and the subsequent region with a steady-state degradation slope. Sample LVL 1.4 was characterized by slight performance decay, and LVL 1.5 was stable under applied AST conditions.

Changes in different overpotential types were analyzed to scrutinize the degradation origin (Figure 4B, Table S3). As can be seen from the overpotentials comparison diagram (Figure 4B), the performance decay in the case of LVL 1.4 was mainly caused by the increase in the kinetic and ohmic overpotentials. It should be noted that in the case of the LVL 1.4 sample, a reversal current occurred during cycling to the LVL (Figure S7), introducing an additional stress factor. Increased degradation under OCV conditions has been reported in terms of AST investigations. Reduction conditions during cycling to the OCV were assumed to cause an enhanced dissolution of Ir[20] and significant cathode degradation in terms of Pt agglomeration and carbon corrosion,[21,22] explained by the work of electrolyzer in a fuel cell mode under conditions of residual gases produced.[33] Meanwhile, the LVL 1.5 protocol, for which no reversal current was observed, resulted in insignificant performance changes, with slight decreases in the kinetic and mass transport overpotentials. Such enhancement in terms of kinetic overpotential during fast cycling was also observed by other researchers and explained by the initial improvement of the catalyst/membrane interface due to the creation of a rougher surface structure,[14] or surface hydroxide layer formation during cycling to lower voltages, associated with a high electrochemical activity.[12,13]

Considering LVL 1.7 and LVL 1.9, obvious mass transport overpotential build-up can be observed after fluctuating high voltage cycling operation associated with the fast bubble nucleation under high current density. The effect of dynamic AST on the mass-transport overpotential is controversially described in previous studies. Some point to the mass-transport overpotential build-up due to increased gas bubble formation under elevated current densities and related degradation processes (delamination, accelerated corrosion, and passivation).[21,26,34] Others imply that mass-transport overpotential was restored to some extent after dynamic AST protocols during cycling to lower voltages because of the decrease in entrapping effect.[12,21] When considering the research conditions (applied loads and cycling frequency), it can be assumed that with an increase in the cycling frequency combined with a high current density and high voltage operation, there is a tendency for an increase in the mass-transport loss accumulation, while a lower cycling frequency will facilitate its partial recovery.

Averaged degradation rates in mV h^{-1}, calculated from the BoT and EoT polarization curves can be seen in Table S4. Negative values, obtained in the LVL 1.5 case, are most likely due to the slight decrease in the kinetic and mass transport overpotential. Both phenomena previously described for the square-wave ASTs with the step duration from a few minutes up to tens of seconds[13,23] seem to be more pronounced in the case of more frequent cycling. To investigate the degradation processes in more detail, impedance spectroscopy results at different voltages were analyzed.

3.2 | Impedance changes

EIS is a powerful tool that can be used to assess the contribution of different resistance types to the overall overpotential. A schematic description of the Nyquist plot semicircles, which occurred at different frequencies
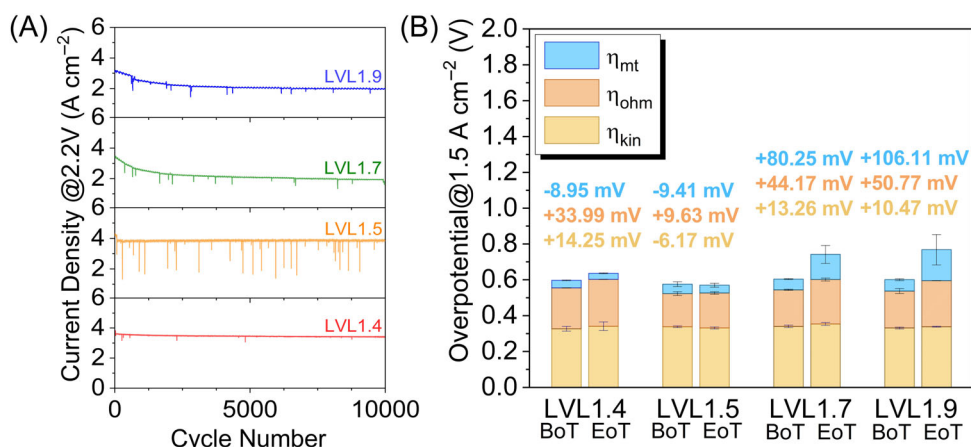

FIGURE 4 Performance changes. (A) Current densities at 2.2 V during the voltage cycling. (B) Overpotential breakdown at 1.5 A cm^{-2}

corresponding to the equivalent circuit elements used in this study, are shown in Data S1 (Figure S8). Considering the activation overpotential, which had the greatest impact in the case of EIS@1.5 V, a small semicircle observed at high frequencies was described as the cathode charge transfer resistance (Figure S8a, $R_{ct,c}$), and a large semicircle at low frequencies was described as the anode charge transfer resistance (Figure S8a, $R_{ct,a}$), considering the sluggish kinetics of the oxygen evolution reaction (OER).[35-38] The real axis intersection point is usually described as an ohmic resistance R_{ohm}, including the electrical resistance of the cell components, ionic resistance of the membrane/ionomer, and interfacial contact resistance between adjacent cell components.

Considering EIS@1.9V, the occurrence of two semicircles was clearly observed. The phenomenological reason for the second semicircle is not clearly understood yet. However, it should be noted that the second semicircle is often explained as arising from mass transport limitation, which occurs due to the covering of the electrode surface with bubbles hindering water access,[39-41] therefore, semicircles are designated as R_{ct} and R_{mt} for the low and high frequency, respectively (Figure S8b).

Analysis of the Nyquist plots (Figure S9 and Tables S5-S8), obtained from the EIS@1.5V (Figure 5A), demonstrate an increase in R_{ohm} for all samples. Given the changes in R_{ohm} after the dynamic AST, degradation processes such as membrane thinning and Ti PTL passivation were frequently observed. The counteracting effect of this degradation processes was described by Founda-Onana et al.[18] At a lower operating temperature (60°C), the prevailing membrane thinning resulted in an increase in performance, while at an increased operating temperature (80°C), the prevailing Ti PTL passivation resulted in performance decay, hindering the membrane thinning. Generally, an increase in R_{ohm} due to the formation of the TiO_2 layer was commonly reported as one of the main reasons for the gradual performance decrease during dynamic AST.[18-21,34] In the case of membrane thinning prevalence, there is an initial performance increase

due to the R_{ohm} decay, however, it will eventually lead to a sudden cell shutdown.[22,25] In addition to the ionic resistance of the membrane/ionomer, R_{ohm} also includes the electrical resistance of the cell components and interfacial contact resistance between adjacent cell components. An increase in R_{ohm} in the case of LVL 1.4 can be triggered by the reversal current occurrence, associated with platinum catalyst degradation and migration toward the anode.[42] This degradation mechanism results in two things: a loss of platinum particles from the cathode and blockage of the anode catalyst surface by cathodic metal deposition. Considering the relatively large cathode catalyst load, the Pt/C degradation mechanism seemed to have more effect on the anode, blocking its surface by cathodic metal deposition, while the loss of Pt particles from the cathode did not have a significant impact (for the given catalyst loading). The scenario, described above, may explain higher increases in the R_{ohm} (Pt deposition in the membrane) and $R_{ct,a}$ in the case of LVL1.4, compared to LVL1.5. In the LVL1.5 protocol, such an increase in the R_{ohm} and $R_{ct,a}$ was not observed.

Analysis of the Nyquist plots measured at 1.9 V demonstrated a substantial increase in the R_{mt} for both LVL 1.7 and LVL 1.9 samples. This increase is associated with delamination of the catalyst/membrane and/or diffuse layer/catalyst interface from intensive gas nucleation and subsequent interface erosion (Figure S10 and Tables S9-S12). A possible explanation may be that the applied AST protocols, with a fast shift in voltages and the high current density operation, triggered changes in bubble growth behavior resulting in interface deterioration. Similar trends for the membrane/catalyst interface deterioration under intense gas bubbling have been reported under dynamic conditions.[19,34] The findings indicate dramatic performance decay due to this degradation mechanism in the case of dynamic operation without cycling to lower voltages (LVL 1.7 and LVL 1.9). To provide more insight into the changes in the electrochemically active area after dynamic AST, CVs at the BoT and EoT were recorded and analyzed.

FIGURE 5 Impedance changes. Impedance components obtained from fitting of Nyquist plots measured at (A) 1.5 V and (B) 1.9 V. The filled area, shaded area, and tranparent area indicate ohmic resistance, high-frequency semicircle resistance, and low-frequency semicircle resistance, respectively
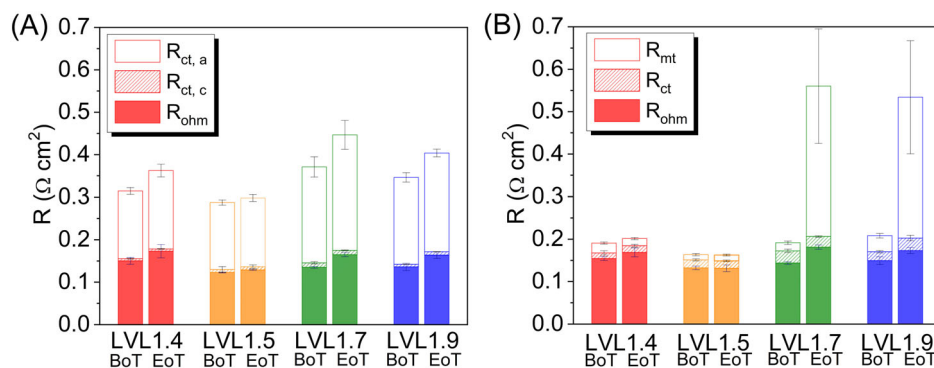
3.3 | Voltammetric charge changes

Changes in the number of active sites under dynamic AST conditions have rarely been investigated. Rozain et al[19] reported a sharp decrease in the low-frequency capacitance (assumed as a representative of the electro-chemical surface area) during the first hours of the dynamic loads, both in the case of the applied AST proto-col and real "solar-type" current profile. The authors attribute this to the stress produced by oxygen nucleation.

In this study, cyclic voltammetry for the BoT mea-surement was conducted three times using three inde-pendently prepared MEAs to avoid introducing an additional degradation source and demonstrate reproduc-ibility between initial measurements. EoT measurements were performed after each applied AST protocol. CVs recorded at 50 mV s^{-1} at the BoT and EoT (Figure 6A) demonstrated the typical CV shape of IrO_2 electrodes in the given voltage range.[19,43] The peak at low voltages (A_1/C_1) may be attributed to O/OH chemisorption,[44] followed by reversible peaks (A_2/C_2) of facile protonation and deprotonation with the formation of $IrO(OH)_2$ or $IrO_2 \cdot H_2O$.[19,44] Subsequent A_3/C_3 peaks are presumably attributed to $IrO_2(OH)$ formed by the oxidation of $IrO(OH)_2$.[44]

Changes in the number of active sites assumed to be proportional to the voltammetric charge density (Q_{total}), obtained by the integration of CVs at different scan rates (10, 30, 50, 70, 100, 200, and 300 mV s^{-1}), using the method proposed by Lodi et al.[45] The corresponding CVs, related to the determination of Q_{outer} and Q_{total}, can be seen in Data S1 (Figure S11). The catalyst layer capaci-tance was evaluated using the CVs by plotting the mea-sured current, which is presumably ascribed only to the surface-controlled capacitive behavior, against the applied scan rate. The obtained voltammetric charge den-sity values and catalyst capacitance values are listed in Table 1. The obtained Q_{total} values are slightly higher than the published data for in situ voltammetric charge evaluation for a single cell (0.43 C cm^{-2}[46] or 0.7 C cm^{-2}[19]). The accessibility value, which indicates the share of easily accessible active sites, was calculated as a Q_{outer}/Q_{total} ratio, as shown in Table 1.

After the applied AST, a decrease in the Q_{total} was observed for samples LVL1.4, LVL 1.7, and LVL1.9, pri-marily due to the decrease in Q_{outer} (Figure 6B). This indicated that morphological changes to the porous struc-ture of the catalytic layer were caused by dynamic loads and a decreasing number of easily available active sites. The obtained accessibility values for these samples also demonstrated a decreasing tendency after the AST. A decrease in Q_{total} was also observed for LVL1.5, however, this was mostly due to the decrease in the Q_{inner}, while Q_{outer} remained almost unchanged. This acts to increase accessibility. Considering that Q_{inner} is related to the number of difficult to access surface regions such as in pores, cracks, and on the grain boundaries, its decreased value may indicate catalyst surface reconstruction by the dynamic operation, exposing more active sites to the
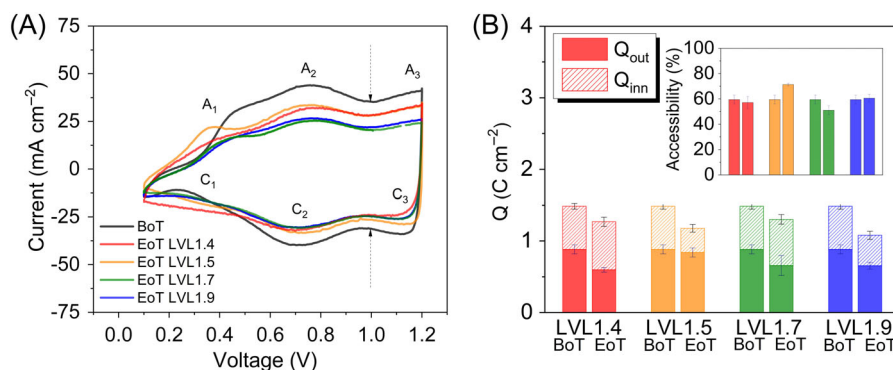

FIGURE 6 Voltammetric charge changes. (A) CVs were recorded at a sweep rate of 50 mV s^{-1} at 80°C, H_2O was supplied to the anode at 5 mL min^{-1}, and humidified H_2 was supplied to the cathode at 50 mL min^{-1}. The potential used to calculate capacitance in anodic and cathodic branches of CVs is marked by arrows. (B) Q_{outer}, Q_{inner}, Q_{total}, and accessibility changes

TABLE 1 Voltammetric charge and double layer capacitance evaluation

Sample	Q_{total} (C cm^{-2})	Q_{inner} (C cm^{-2})	Q_{outer} (C cm^{-2})	Accessibility, Q_{outer}/Q_{total} (%)	C (F cm^{-2})
BoT	1.48 ± 0.033	0.60 ± 0.062	0.88 ± 0.040	59.49 ± 3.520	0.77 ± 0.0090
LVL1.4 EoT	1.23 ± 0.018	0.55 ± 0.007	0.70 ± 0.012	56.12 ± 0.287	0.59 ± 0.0020
LVL1.5 EoT	1.16 ± 0.006	0.32 ± 0.030	0.84 ± 0.024	70.77 ± 2.524	0.59 ± 0.0120
LVL1.7 EoT	1.21 ± 0.139	0.59 ± 0.130	0.62 ± 0.078	51.05 ± 6.560	0.51 ± 0.0001
LVL1.9 EoT	1.08 ± 0.009	0.42 ± 0.048	0.65 ± 0.056	60.61 ± 4.800	0.51 ± 0.0020

electrolyte.[19,47,48] This results in a slight increase in accessibility for LVL1.5.

3.4 | Post-operation analysis

Membrane chemical degradation, namely thinning via radical attack, is widely known as one of the main degradation mechanism under applied dynamic AST conditions.[12,18,22,24,25] Grigoriev et al[25] and Founda-Onana et al[18] reported higher F^- release on the cathode under dynamic AST, which is in line with the radical attack mechanism, according to which O_2 crossover from the anode to the cathode causes the formation of hydrogen peroxide with subsequent formation of radicals via the Fenton reaction. Fouda-Onana et al[18] also indicated a temporary positive effect of membrane thinning on performance during dynamic operation, which will lead to subsequent cell failure under prolonged operation.

Ir dissolution and migration to the cathode under dynamic conditions, revealed by scanning transmission electron microscopy imaging of the membrane/anode interface,[13,20,25] introduced an additional chemical membrane degradation mechanism, namely metal poisoning. Based on the mechanism described by Grigoriev et al,[25] cationic species, which occur after catalyst dissolution, migrate toward the cathode due to the electric field, and subsequently react with the dissolved hydrogen, being reduced into insoluble particles.

The influence of mechanical degradation, an additional membrane degradation mechanism induced by MEA between two Ti PTLs, was investigated by Babic et al,[13] revealing an increased F^- release rate and frequent cracks and fissures in the catalyst layer after the operation.

To investigate the morphological changes after AST, cross-sectional scanning electron microscopy (SEM) images of the MEA were taken (Figure 7). Additionally, SEM images of the freeze-fractured CCMs were obtained to evaluate the membrane thinning effect more precisely and to better understand delamination at the catalyst/membrane and/or diffuse layer/catalyst interface (Figure S12). The averaged membrane thicknesses were calculated and summarized in Table S13. The initial MEA measurement (BoT) was performed after the conditioning procedure to take into account membrane swelling and assembling influence. Another significant factor that influences the R_{ohm} along with the membrane resistance is Ti PTL passivation. XPS analysis was performed to provide a comparative assessment of the Ti passivation degree (Figure S13 and Table S14).[49,50]

A significant thinning degree was observed with an increase in the LVL (which implies cycling operation at higher loads). The effect of the applied current density on the gas crossover and subsequent membrane thinning was investigated by Chandesris et al, revealing a maximum F^- release rate of about 0.4 A cm^{-2} in a current density range up to 1.2 A cm^{-2}. Lower membrane degradation at lower current density was explained by the high H_2O_2 concentration and its influence on the predominance reaction. At current densities higher than 0.4 A cm^{-2}, the decreased F^- release rate was explained by the decreased molar concentration of oxygen at the cathode.

However, applied voltages and consequent current densities in this study are significantly high, which could
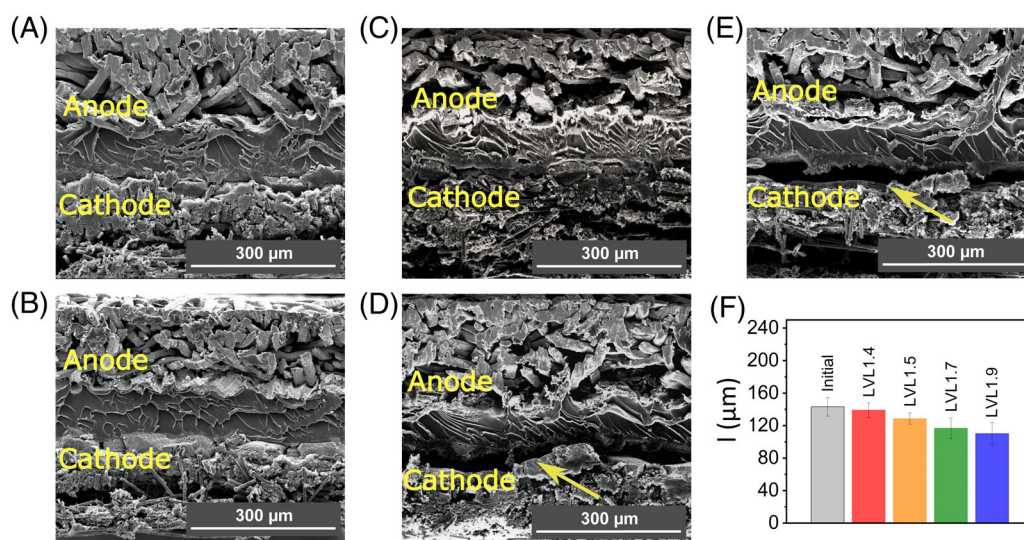

FIGURE 7 Cross-section SEM images of the MEA for (A) BoT, (B) LVL1.4 EoT, (C) LVL1.5 EoT, (D) LVL1.7 EoT, and (E) LVL1.9 EoT. (F) Comparison of the averaged membrane thicknesses

magnify the influence of such mechanisms related to local temperature increase and widening of the water channels within the membrane in conjunction with the increased diffusion coefficient. The above conditions could lead to increased oxygen permeation and, as a consequence, significant membrane thinning. Additionally, protocols LVL 1.7 and LVL 1.9, due to an increase in the LVL and at the same time maintaining the same sweep rate (150 mV s^{-1}), have a shorter step duration, which may influence the bubble nucleation, growth, and detachment behavior, resulting in the deterioration of the membrane/catalyst interface.

Despite the observed membrane thinning, decay in the R_{ohm} and an corresponding increase in performance was not observed, indicating the prevailing influence of the Ti PTL passivation. Additionally, considering that R_{ohm} also includes interfacial contact resistance between adjacent cell components, the observed delamination of catalyst/membrane and/or diffuse layer/catalyst interface (Figure 7D,E) may hinder the temporary positive effect of membrane thinning.

The deconvoluted XPS spectra of the Ti felt surface can be seen in Figure S13. The XPS peak positions and quantified peak areas are summarized in Table S14. The deconvoluted Ti 2p XPS spectra showed two major doublets (Figure S13): a brown-colored doublet at 458.8 to 459.0 eV ($2p_{3/2}$) and 464.5 to 464.7 eV ($2p_{1/2}$), and a gray-colored doublet at 453.9 to 454.2 eV ($2p_{3/2}$) and 460.0 eV ($2p_{1/2}$), which are indicative of Ti(IV) oxide and Ti metal, respectively. All Ti 2p spectra are dominated by the Ti(IV) oxide peak, which indicates the prevalence of the TiO$_2$ passivation layer on the Ti felt surface. For the quantitative comparison of Ti passivation degree, the relative peak area ratio was calculated and summarized as the bar plot in Figure S13f. Considering that the "Initial" sample was considerably passivated with an oxide layer (92.6%), most of the passivation layer could be formed during the pre-conditioning procedure. After the ASTs, the oxide ratio on the surface of Ti felt remained almost unchanged (92.4%-93.3%), indicating that the resulting passivation layer was not a matter of sample-to-sample differences.

4 | CONCLUSIONS

In this study, dynamic load cycling was suggested as the AST protocol for renewable energy-powered PEMWE, which combines the fluctuating behavior of renewable power and high loads essential to reduce the H$_2$ production costs. The AST protocol with a lower cycling limit of 1.4 V resulted in performance decay in all overpotential regions, presumably triggering cathode catalyst

degradation due to reversal current occurrence. In this case, the observed degradation rate was 1 mV h^{-1} at 1 A cm^2. On the contrary, LVL 1.5 cycling showed a negative degradation slope of -0.22 mV h^{-1} at 1 A cm^2, attributed to membrane thinning and structural improvements on the catalyst/membrane interface. However, such changes may eventually lead to sudden cell shutdown during long-term operation. Notably, high load (LVL 1.7 and LVL 1.9) cycling resulted in a significant overpotential increase in the mass transport region. A probable reason is a change in bubble growth behavior during a fast voltage shift, resulting in interface deterioration between the catalyst/membrane and/or diffuse layer/catalyst interfaces.

These findings provide valuable insight into the degradation processes triggered by dynamic cycling with various high loads and suggest guidelines for the AST protocol applicable to renewable energy-powered PEMWE. Additional post characterizations can be useful for guiding subsequent material development to minimize degradation processes, specifically triggered by dynamic loads.

CONFLICT OF INTEREST
The authors declare no conflicts of interest.

ENDNOTE
* Rakousky et al[21] and Siracusano et al[12] used the term "reversible losses" to indicate those losses that can be restored by interrupting the current and it is assumed that it is, for example, some part of the mass transport losses. This footnote is made not to confuse with the reversible voltage V_{rev}.

DATA AVAILABILITY STATEMENT
The data that support the findings of this study are available from the corresponding author upon reasonable request.

ORCID
Bora Seo https://orcid.org/0000-0002-4387-0706

REFERENCES

1. Buttler A, Spliethoff H. Current status of water electrolysis for energy storage, grid balancing and sector coupling via power-to-gas and power-to-liquids: a review. *Renew Sust Energ Rev.* 2018;82:2440-2454. doi:10.1016/j.rser.2017.09.003

2. Shiva Kumar S, Himabindu V. Hydrogen production by PEM water electrolysis – a review. *Mater Sci Energy Technol.* 2019; 2(3):442-454. doi:10.1016/j.mset.2019.03.002

3. Ayers K. The potential of proton exchange membrane–based electrolysis technology. *Curr Opin Electrochem.* 2019;18:9-15. doi:10.1016/j.coelec.2019.08.008

4. Aricò AS, Siracusano S & Briguglio N

5. Clarke RE, Giddey S, Badwal SPS. Stand-alone PEM water electrolysis system for fail safe operation with a renewable energy source. *Int J Hydrog Energy.* 2010;35(3):928-935. doi:10.1016/j.ijhydene.2009.11.100

6. Privitera SMS, Muller M, Zwaygardt W, et al. Highly efficient solar hydrogen production through the use of bifacial photovoltaics and membrane electrolysis. *J Power Sources.* 2020;473: 228619. doi:10.1016/j.jpowsour.2020.228619

7. Dr Magnus Skinlo Thomassen Next Generation PEM Electrolyser for Sustainable Hydrogen Production. 2013. http://www.sartre-project.eu/en/publications/Documents/SARTRE_Final-Report.pdf

8. Thomassen MS. Novel Materials and System Designs for Low Cost, Efficient and Durable PEM Electrolysers. 2001. https://cordis.europa.eu/docs/results/300/300081/final1-electrohypem-final-publishable-summary-report-15-09-2015-f.pdf

9. Aricò DAS. Enhanced Performance and Cost-Effective Materials for Long-Term Operation of PEM Water Electrolysers Coupled to Renewable Power Sources. 2015. https://cordis.europa.eu/docs/results/300/300081/final1-electrohypem-final-publishable-summary-report-15-09-2015-f.pdf

10. Scheffer K. Specifications of Pilot Test 1/Use Case 1. 2017. https://www.h2future-project.eu/images/Publications/D2.1_H2F_WP2.pdf

11. Hegge F, Lombeck F, Cruz Ortiz E, et al. Efficient and stable low iridium loaded anodes for PEM water electrolysis made possible by nanofiber interlayers. *ACS Appl Energy Mater.* 2020;3(9):8276-8284. doi:10.1021/acsaem.0c00735

12. Siracusano S, Trocino S, Briguglio N, Pantò F, Aricò AS. Analysis of performance degradation during steady-state and load-thermal cycles of proton exchange membrane water electrolysis cells. *J Power Sources.* 2020;468:228390. doi:10.1016/j.jpowsour.2020.228390

13. Babic U, Tarik M, Schmidt TJ, Gubler L. Understanding the effects of material properties and operating conditions on component aging in polymer electrolyte water electrolyzers. *J Power Sources.* 2020;451:227778. doi:10.1016/j.jpowsour.2020.227778

14. Alia SM, Rasimick B, Chilan Ngo KC, et al. Activity and durability of iridium nanoparticles in the oxygen evolution reaction. *ECS Meet Abstr.* 2016;163(11):F3105-F3112. doi:10.1149/MA2015-02/37/1456

15. Aßmann P, Gago AS, Gazdzicki P, Friedrich KA, Wark M. Toward developing accelerated stress tests for proton exchange membrane electrolyzers. *Curr Opin Electrochem.* 2020;21:225-233. doi:10.1016/j.coelec.2020.02.024

16. Spöri C, Kwan JTH, Bonakdarpour A, Strasser P. The stability challenges of oxygen evolving electrocatalysts: towards a common fundamental understanding and mitigation of catalyst degradation. *Angew Chem.* 2017;129(22):6088-6117. doi:10.1002/ange.201608601

17. Price E. Durability and degradation issues in PEM electrolysis cells and its components: the second international workshop organised by the novel EU-funded programme. *Johnson Matthey Technol Rev.* 2017;61(1):47-51. doi:10.1595/205651317X693732

18. Fouda-Onana F, Chandesris M, Médeau V, Chelghoum S, Thoby D, Guillet N. Investigation on the degradation of MEAs for PEM water electrolysers part I: effects of testing conditions on MEA performances and membrane properties. *Int J Hydrog Energy.* 2016;41(38):16627-16636. doi:10.1016/j.ijhydene.2016.07.125

19. Rozain C, Mayousse E, Guillet N, Millet P. Influence of iridium oxide loadings on the performance of PEM water electrolysis cells: part II - advanced oxygen electrodes. *Appl Catal B Environ.* 2016;182:123-131. doi:10.1016/j.apcatb.2015.09.011

20. Weiß A, Siebel A, Bernt M, Shen T-H, HAG VT. Impact of intermittent operation on lifetime and performance of a PEM water electrolyzer. *J Electrochem Soc.* 2019;166(8):F487-F497. doi:10.1149/2.0421908jes

21. Rakousky C, Reimer U, Wippermann K, et al. Polymer electrolyte membrane water electrolysis: restraining degradation in the presence of fluctuating power. *J Power Sources.* 2017;342: 38-47. doi:10.1016/j.jpowsour.2016.11.118

22. Li N, Araya SS, Kær SK. Investigating low and high load cycling tests as accelerated stress tests for proton exchange membrane water electrolysis. *Electrochim Acta.* 2021;370: 137748. doi:10.1016/j.electacta.2021.137748

23. Frensch SH, Fouda-Onana F, Serre G, Thoby D, Araya SS, Kær SK. Influence of the operation mode on PEM water electrolysis degradation. *Int J Hydrog Energy.* 2019;44(57):29889-29898. doi:10.1016/j.ijhydene.2019.09.169

24. Kasian O, Grote JP, Geiger S, Cherevko S, Mayrhofer KJJ. The common intermediates of oxygen evolution and dissolution reactions during water electrolysis on iridium. *Angew Chem Int Ed.* 2018;57(9):2488-2491. doi:10.1002/anie.201709652

25. Grigoriev SA, Dzhus KA, Bessarabov DG, Millet P. Failure of PEM water electrolysis cells: case study involving anode dissolution and membrane thinning. *Int J Hydrog Energy.* 2014; 39(35):20440-20446. doi:10.1016/j.ijhydene.2014.05.043

26. Papakonstantinou G, Algara-Siller G, Teschner D, Vidaković-Koch T, Schlögl R, Sundmacher K. Degradation study of a proton exchange membrane water electrolyzer under dynamic operation conditions. *Appl Energy.* 2020;280:115911. doi:10.1016/j.apenergy.2020.115911

27. Natural Resources Canada. High-resolution solar radiation datasets. High-Resolution Solar Radiation Datasets. 2020. Accessed October 21, 2021. https://www.nrcan.gc.ca/energy/renewable-electricity/solar-photovoltaic/18409

28. CNL에너지: Carbon & Fuelcell. http://cnl.co.kr/cnl/products/service.php?PHPSESSID=9c0397fe21b348f01ce3a1cea6c75372

29. FuelCell store. https://www.fuelcellstore.com/sigracet-39bc

30. Ojong ET, Kwan JTH, Nouri-Khorasani A, Bonakdarpour A, Wilkinson DP, Smolinka T. Development of an experimentally validated semi-empirical fully-coupled performance model of a PEM electrolysis cell with a 3-D structured porous transport layer. *Int J Hydrog Energy.* 2017;42(41):25831-25847. doi:10.1016/j.ijhydene.2017.08.183

31. Schmidt G, Suermann M, Bensmann B, Hanke-Rauschenbach R, Neuweiler I. Modeling overpotentials related to mass transport through porous transport layers of PEM water electrolysis cells. *J Electrochem Soc.* 2020;167(11):114511. doi:10.1149/1945-7111/aba5d4

32. Pushkarev AS, Pushkareva IV, Solovyev MA, et al. On the influence of porous transport layers parameters on the performances of polymer electrolyte membrane water electrolysis cells. *Electrochim Acta.* 2021;399:139436. doi:10.1016/j.electacta.2021.139436

33. Grigoriev SA, Bessarabov DG, Fateev VN. Degradation mechanisms of mea characteristics during water electrolysis in solid polymer electrolyte cells. *Russ J Electrochem.* 2017;53(3):359-365. doi:10.1134/S1023193517030065

34. Rakousky C, Keeley GP, Wippermann K, Carmo M, Stolten D. The stability challenge on the pathway to high-current-density polymer electrolyte membrane water electrolyzers. *Electrochim Acta.* 2018;278:324-331. doi:10.1016/j.electacta.2018.04.154

35. Ban HJ, Kim MY, Kim D, et al. Electrochemical characteristics of solid polymer electrode fabricated with low IrO_2 loading for water electrolysis. *J Electrochem Sci Technol.* 2019;10(1):22-28. doi:10.5229/JECST.2019.10.1.22

36. Siracusano S, Hodnik N, Jovanovic P, et al. New insights into the stability of a high performance nanostructured catalyst for sustainable water electrolysis. *Nano Energy.* 2017;40:618-632. doi:10.1016/j.nanoen.2017.09.014

37. Su H, Linkov V, Bladergroen BJ. Membrane electrode assemblies with low noble metal loadings for hydrogen production from solid polymer electrolyte water electrolysis. *Int J Hydrog Energy.* 2013;38(23):9601-9608. doi:10.1016/j.ijhydene.2013.05.099

38. Siracusano S, Trocino S, Briguglio N, Baglio V, Aricò AS. Electrochemical impedance spectroscopy as a diagnostic tool in polymer electrolyte membrane electrolysis. *Materials.* 2018;11(8):1368. doi:10.3390/ma11081368

39. Lettenmeier P, Kolb S, Sata N, et al. Comprehensive investigation of novel pore-graded gas diffusion layers for high-performance and cost-effective proton exchange membrane electrolyzers †. *Energy Environ Sci.* 2017;10:2521-2533. doi:10.1039/c7ee01240c

40. Dedigama I, Angeli P, Ayers K, et al. In situ diagnostic techniques for characterisation of polymer electrolyte membrane water electrolysers - flow visualisation and electrochemical impedance spectroscopy. *Int J Hydrog Energy.* 2014;39(9):4468-4482. doi:10.1016/j.ijhydene.2014.01.026

41. Immerz C, Bensmann B, Trinke P, Suermann M, Hanke-Rauschenbach R. Local current density and electrochemical impedance measurements within 50 cm single-channel PEM electrolysis cell. *J Electrochem Soc.* 2018;165(16):F1292-F1299. doi:10.1149/2.0411816jes

42. Feng Q, Yuan XZ, Liu G, et al. A review of proton exchange membrane water electrolysis on degradation mechanisms and mitigation strategies. *J Power Sources.* 2017;366:33-55. doi:10.1016/j.jpowsour.2017.09.006

43. Montero MA, de Chialvo MRG, Chialvo AC. Effects of the electrochemically grown hydrous oxide on the hydrogen electrode reaction on iridium electrode. *J Electroanal Chem.* 2016;783:106-111. doi:10.1016/j.jelechem.2016.11.037

44. Cherevko S, Geiger S, Kasian O, Mingers A, Mayrhofer KJJ. Oxygen evolution activity and stability of iridium in acidic media. Part 2. - electrochemically grown hydrous iridium oxide. *J Electroanal Chem.* 2016;774:102-110. doi:10.1016/j.jelechem.2016.05.015

45. Lodi G, Sivieri E, De Battisti A, Trasatti S. Ruthenium dioxide-based film electrodes - III. Effect of chemical composition and surface morphology on oxygen evolution in acid solutions. *J Appl Electrochem.* 1978;8(2):135-143. doi:10.1007/BF00617671

46. Zhao S, Yu H, Maric R, et al. Calculating the electrochemically active surface area of iridium oxide in operating proton exchange membrane Electrolyzers. *J Electrochem Soc.* 2015;162(12):F1292-F1298. doi:10.1149/2.0211512jes

47. Felix C, Bladergroen BJ, Linkov V, Pollet BG, Pasupathi S. Ex-situ electrochemical characterization of IrO_2 synthesized by a modified Adams fusion method for the oxygen evolution reaction. *Catalysts.* 2019;9(4):318. doi:10.3390/catal9040318

48. Genova-Koleva RV, Alcaide F, Álvarez G, et al. Supporting IrO_2 and $IrRuO_x$ nanoparticles on TiO_2 and Nb-doped TiO_2 nanotubes as electrocatalysts for the oxygen evolution reaction. *J Energy Chem.* 2019;34:227-239. doi:10.1016/j.jechem.2019.03.008

49. Bystron T, Vesely M, Paidar M, et al. Enhancing PEM water electrolysis efficiency by reducing the extent of Ti gas diffusion layer passivation. *J Appl Electrochem.* 2018;48(6):713-723. doi:10.1007/s10800-018-1174-6

50. Liu C, Shviro M, Gago AS, et al. Exploring the Interface of skin-layered titanium fibers for electrochemical water splitting. *Adv Energy Mater.* 2021;11(8):2002926. doi:10.1002/aenm.202002926

SUPPORTING INFORMATION

Additional supporting information may be found in the online version of the article at the publisher's website.